LLNL-JRNL-2004894

Lawrence Livermore National Laboratory

The influence of laser power modulation on melt pool dynamics in laser powder bed fusion

M Strantza, D Rosas, G Guss, M Nielsen, J Lee, J Hammons, A Martin, N Calta, I Matthews, T Willey

December 2025

Journal of Applied Physics

Disclaimer

This work performed under the auspices of the U.S. Department of Energy by Lawrence Livermore National Laboratory under Contract DE-AC52-07NA27344.

The influence of laser power modulation on melt pool dynamics in laser powder bed fusion

NP Calta,* AA Martin, JA Hammons, MH Nielsen, DL Rosas, M Strantza, GM Guss, MJ Matthews, TM Willey, JRI Lee

Lawrence Livermore National Laboratory, Livermore, CA

*calta1@llnl.gov

Abstract

While the majority of laser powder bed fusion metal additive manufacturing uses a continuous wave (CW) laser heat source, some commercial applications of laser powder bed fusion (LPBF) additive manufacturing instead involve the modulation of the laser power on tens-of-microsecond timescales as an adjustable process variable. This article reports the use of *in situ*, high speed X-ray and optical imaging to probe melt pool fluid flow, defect formation, and nearby powder motion during LPBF with both modulated and CW laser heat sources. We observe melt pool dynamics unique to modulated laser melting even at very high duty cycles that are related to fluctuations in vapor depression depth, complex pore formation mechanisms, and changes to denudation physics when compared to CW melting. These behaviors are present in Ti-6Al-4V, 316L stainless steel, and AL1100 alloys but vary slightly as a function of material, indicating a substantial dependence on the viscosity and surface tension of the liquid metal. While high duty cycles produce weld tracks of comparable quality to CW melting, lower duty cycles introduce substantial defect concentrations. At intermediate duty cycles, careful control of modulation parameters can repeatably and precisely yield one pore per laser pulse, suggesting a method for intentionally inserting engineered porosity at specific sites during an LPBF build.

I. Introduction

Laser-based materials processing is increasingly used in industrial settings for advanced manufacturing techniques such as laser cutting, drilling, welding, or laser-based additive manufacturing techniques such as laser powder bed fusion (LPBF), sometimes also called selective laser melting (SLM). With some exceptions, material removal approaches generally use short (nanoseconds or shorter) pulse lasers to remove material via ablation and impart a shock to the material,[1] while joining and additive manufacturing approaches usually use continuous wave (CW) lasers that are either operated continuously or modulated with relatively long (>10 μs) pulses to either form a continuous melt pool or series of spot welds.[2-5] Consequently, a great deal is known about melt pool fluid dynamics in the CW regime relevant to most laser welding and additive manufacturing applications[6-13] and there is also extensive literature relating to material response under short pulse irradiation.[1, 14-18] In contrast, there is far less understanding of material behavior when exposed to a series of longer laser pulses where the laser power fluctuations are on the order of tens of microseconds, especially with respect to subsurface dynamics during laser melting. These dynamics are relevant both to additive manufacturing as well as some laser material removal methods.[19]

Although unmodulated CW laser melting is the most prevalent heat source for LPBF fabrication approaches, the use of modulated CW lasers to achieve microsecond pulses at kHz repetition rates has also been demonstrated. Builds using long pulse, modulated CW lasers can achieve high spatial resolution, especially in thin walls or small struts.[4, 20-23] This ability to achieve fine features has been attributed to smaller or narrower melt pool sizes achieved by tuning the energy deposition with laser pulsing.[24] Pulse parameters also influence nitrogen uptake during part fabrication under nitrogen atmospheres.[25] Varying pulse duration provides an approach for controlling the as-solidified microstructure by influencing the heat input and consequently changing solidification cell sizes.[26, 27] In some instances, parts built with a laser pulsing strategy yield different grain sizes and phase fractions than parts made with CW processing.[28] In addition to varying the thermal gradients, the melt generally penetrates deeper into the substrate for pulsed laser welding than for CW welding at equivalent energy densities,[29] which alters the shape of the weld pool and further modifies the solidification conditions that ultimately determine microstructure. The laser pulse duration also has a substantial influence on part density with longer pulses generally producing higher-density parts,[30, 31] so the range of pulse durations that can be exploited to tune the solidification microstructure is limited by the competing need to produce fully dense parts. While single-track studies have observed changes in melt morphology as a function of pulse duration[32] and optical imaging studies have observed melt surface dynamics and spatter behavior,[24] it is not clear how these dynamics would directly lead to the bulk porosity that leads to low-density parts produced in pulsed LPBF.

High speed, *in situ* synchrotron X-ray imaging and diffraction are powerful tools to probe subsurface dynamics during laser melting, especially with regard to pore formation mechanisms and bulk phase transitions or cooling rates.[33-36] High speed X-ray imaging experiments have observed a variety of different defect formation mechanisms during LPBF,[37-41] quantified vapor depression geometry as a function of process parameters,[42-45] correlated subsurface melt pool behavior with spatter ejection,[46]

observed fluid flow in LPBF and welding,[47, 48] and correlated pore formation with process monitoring signatures.[49-52] Such studies have provided a great deal of insight into the detailed physics that govern the laser-material interaction in LPBF and laser welding, but the vast majority of these studies use CW laser melting, although work by Shevchik *et al*[49] and Hojjatzadeh *et al*[53] study melt pool behavior with a modulated build laser. Tsukamoto *et al* used high speed radiography to study long pulsed laser welding, but their work used a CO_2 laser at substantially different energy densities than those relevant for LPBF.[54] In this article, we use high speed X-ray imaging to systematically investigate melt pool behavior in long pulse, high repetition rate laser melting under conditions used in LPBF. We compliment observations from X-ray imaging with optical imaging to obtain a complete picture of how pulsing the laser can substantially change melt pool dynamics and pore formation mechanisms when compared to CW LPBF.

II. Materials and Methods

A. In situ X-ray imaging

The laser melting experiments used a custom LPBF testbed system designed for use at synchrotron facilities.[40] The system uses a 1070 nm continuous wave Yb-fiber laser (IPG YLR-500) focused to a Gaussian beam diameter (D4σ) of ~ 50 μm at the sample surface. This laser has a rise time of ~ 20 μs and a maximum modulation frequency of 50 kHz. Laser power was modulated via a custom field programmable gate array (FPGA)-based control scheme, and pulse widths were specified with square wave Transistor-Transistor Logic (TTL) pulses commanding the laser to fire at a specified frequency and pulse duration. The actual pulse format (laser power as a function if time) was measured with a photodiode bandpassed to collect scattered laser light when firing the laser into a beam dump. Figure 1 compares the commanded pulse shape and measured pulse shape for a square wave at a peak power of 200 W. The commanded power is plotted as the voltage signal provided to the laser that corresponds to a 200 W power output. There is a non-negligible difference between the commanded and actual pulse shape. This difference varies as a function of modulation frequency and duty cycle/pulse duration, with a few notable trends. First, the actual laser power does not drop all the way to zero in high duty cycle cases (Figure 1a, Supplemental Figures S1 and S2), above 80% duty cycle at 10 kHz and above 60% duty cycle at 20 kHz. Second, at lower duty cycles and correspondingly shorter laser pulses, the peak laser power is not as high as the powers reached in the higher duty cycle cases, especially at 20 kHz (Figure 1c). Finally, behavior during the laser rise, when the pulse is starting, includes a very brief power spike well above the maximum commanded laser power at low duty cycle for 10 kHz repetition rates, very similar to behavior when the laser initially fires in CW operation (Figure 1b, Supplemental Figure S3). This behavior does not occur at higher duty cycle and is less consistent at 20 kHz modulation. These spikes are very brief and the conditions under which they occur do not exhibit unique behavior, so we do not believe these power spikes substantially influence the dynamics described in this manuscript.

For each experiment, the laser was scanned to produce a 3 mm melt track, and all imaging data was collected near the middle of the track after the melt pool had reached steady state. Every experiment used an atmosphere of Ar gas at approximately atmospheric pressure. For experiments with powder,

a ~50 μm thick powder layer was spread with a razor blade on top of the substrate and contained by glassy carbon windows on each side of the substrate. For bare plate melting experiments the substrate plates were clamped directly to the aluminum alloy sample holder without glassy carbon windows. Substrates are 500 μm thick, which is sufficiently wide to eliminate the influence of thermal boundary conditions on melt pool dynamics as illustrated in Calta *et al.*[34]

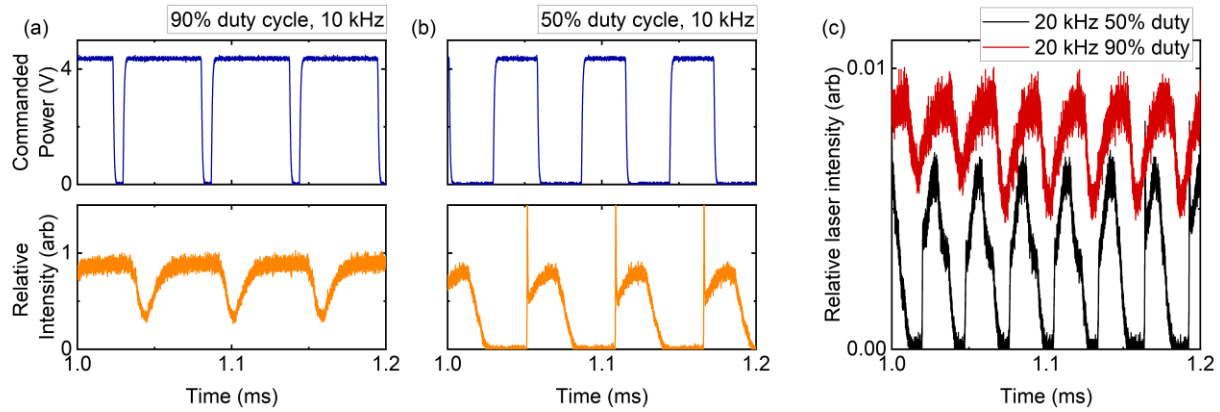

Figure 1. Comparison of commanded and actual laser pulse formats. (a) Commanded power and measured laser intensity for 10 kHz, 90% duty cycle. (b) Commanded power and measured laser intensity for 10 kHz, 50% duty cycle. (c) Comparison of measured laser intensity at 20 kHz for 90% and 50% duty cycle.

Transmission X-ray imaging was performed at beamline 32-ID of the Advanced Photon Source at Argonne National Laboratory. The unattenuated beam from a U18 undulator in 24 bunch mode was used for all measurements, yielding a peak X-ray energy of ~24.4 keV. The X-rays were detected by a scintillator-based fast detector system composed of a 100 μm thick LuAg:Ce scintillator (Crytur) to convert the X-ray photons to visible light, a turning mirror to steer the visible light out of the X-ray beam path, a 20× magnification objective lens (0.42 NA, Mitutoyo) and a 1× tube lens. Images were collected using a Photron SA-Z high speed camera with an exposure time of 2.5 μs and 50.4 kfps frame rate. This camera has 20 × 20 μm^2 pixels, yielding an effective pixel size of 1 × 1 μm^2/pixel. Since the frame rate of the detector is significantly slower than the time between X-ray pulses in 24 bunch mode, the detection system was not synchronized with the X-ray pulse train.

B. X-ray image data analysis

X-ray images were analyzed as absorption difference images to enhance contrast. These absorption difference images for each frame (D_t) were calculated via equation 1:

$$D_t = \frac{\ln A_t}{\ln A_0} \qquad [1]$$

Where A_t is the as-collected image for a given time point t and A_0 is an image of the sample collected prior to laser melting. Pore identification used difference images from after laser melting and averaged multiple frames to reduce noise. Pores were counted manually from these images. Visual inspection

of the corresponding *in situ* laser melting videos confirmed that these pores were formed by the laser processing method and not some other mechanism.

Vapor depression depth measurements were conducted for a subset of laser melting conditions and were only performed for bare plate melting data sets, to reduce uncertainty in the location of the substrate surface induced by the presence of powder. Depths were measured manually by measuring the distance between the location of the substrate surface and the lowest point in the vapor depression. An example of an X-ray image with annotations showing vapor depression and divot depth measurements is shown in the supporting information, Figure S4. The bottom of the vapor depression could be identified with ~ 5 pixel (5 μm) absolute accuracy due to phase contrast, which increases the contrast but reduces the spatial resolution at material interfaces. The location of the top of the substrate could be identified with slightly better absolute accuracy, leading to a conservative estimate of the absolute uncertainty of ~8-10 μm. Since these uncertainties are systematic, the relative uncertainty is estimated to be smaller, on the order of a 3-5 μm. Vapor depression depth was complicated in low duty cycle cases because of ambiguities as to when the material was fully solidified. The vapor depression measurements presented here exclude solidified divots that remain present on the material surface after laser melting, but this distinction is difficult to discern so it is possible that in some frames, a solidified divot was inadvertently classified as a dynamic vapor depression.

C. Metallography

The weld track regions were sheared from the larger substrate, then cut perpendicular to the scan direction using a LECO Vari-cut VC-50 low speed diamond saw. The cut face was mounted with cold mounting epoxy (Streuers Epo-fix resin), then ground down to 1200 grit with an Allied High Tech MetPrep 3, followed by polishing in three diamond suspensions with nylon cloth (6, 3, and 1 μm diamond particles). Finally, the samples were finished with vibratory polishing (Buehler vibromet) with the 1 μm diamond suspension followed by a 0.05 μm colloidal silica final polish. Stainless steel samples were etched electrolytically with a 10:1 water/oxalic acid mixture at 6V for 30 seconds each. Ti-64 samples were not etched. The samples were coated with a 10 nm film of AuPd to reduce charging in a Leica EM ACE600. Scanning electron microscope (SEM) images were collected at 15 kV in mapping mode using a Phenom ProX desktop SEM equipped with a solid state backscatter detector.

D. In situ optical imaging

Complimentary high speed optical imaging experiments were performed to study powder denudation at longer length scales than can be observed in the high speed X-ray images, which have a limited field of view and only observe 2D projections. These experiments used a similar laser melting system to those described in the X-ray imaging section, with some differences to facilitate optical imaging rather than X-ray imaging. The substrate was a 1 inch diameter circular build plate with a 90 μm thick powder layer, and the experiment was conducted outside a vacuum chamber to permit access of visible light optics. A constant cross-flow of Ar gas was used to maintain an inert atmosphere. The experiments used a variety of duty cycles at both 10 kHz and 20 kHz modulation with 100 W peak laser power and

a scan speed of 1 m/s, a ~50 μm Gaussian beam diameter (D4σ), and Ti-64 as the material. High speed optical images were collected by a Photron SA-Z camera coupled to an Infinity K2 Close-Focus Objective (CF-3). These data were recorded at 20 kfps with an exposure time of 1 μs, and the build surface was illuminated using a 810-nm pulsed laser with 500-W peak power (Cavitar, model Cavilux HF) using a pulse duration of 0.95 μs. A 10 nm bandpass filter was used to remove melt pool incandescence. These experiments provide images with spatial resolution on the same order of magnitude of the powder particles, so while individual particle motion cannot be determined the bulk denudation behavior is visible. Immediately after melting experiments, the denudation zones from the series of single tracks were measured via optical microscopy with a Keyence VR3000 microscope to obtain measurements of the denudation zone from each scan. These measurements averaged the denudation zone width at 5 separate points along the track, which were manually selected at approximately uniform intervals away from the start and end of the track where transient effects influence denudation behavior.

III. Results and Discussion

A. Pore formation as a function of duty cycle and frequency

Melt pool fluid flow behavior varies significantly as a function of duty cycle (or, equivalently, pulse duration) and modulation frequency. Here, we present laser pulse parameters by giving peak power, commanded duty cycle, and modulation frequency. From our experiments, we observe three distinct regimes of material behavior as a function of duty cycle, which we categorize based on defect formation behavior. The thresholds between these regimes vary as a function of peak laser power, as expected due to the strong dependence of keyhole physics on the laser input energy, but also the modulation frequency. The frequency and duty cycle dependence suggest that the amount of time *between* laser pulses is the most important parameter that governs pore formation dynamics that arise due to laser power modulation on the timescale of 10s of microseconds. Two key parameters governing these pore formation dynamics are fluid flow, discussed in more detail below, and thermal diffusion. As a starting point to understand thermal effects, we estimate the thermal diffusion length in this scenario, where the laser is represented as a Gaussian heat source.[55] This can be written as:

$$L = \sqrt{4D\tau} \qquad [2]$$

Where L is the diffusion length, D is thermal diffusivity, and τ is the thermal diffusion time. For this estimate, we use the laser off time for τ, to estimate thermal effects and transport between laser pulses, and $D = 5.6 \times 10^{-6}\ m^2\ s^{-1}$ for Ti-64 at 1500 K.[56] These values range from between ~10 μm and ~46 μm over the range of modulation parameters explored in this study and corresponds to travel distances between 5 μm and 95 μm during the nominal laser off time. These calculated values are compared in Figure 2a, and cross over at ~ 75% duty cycle.

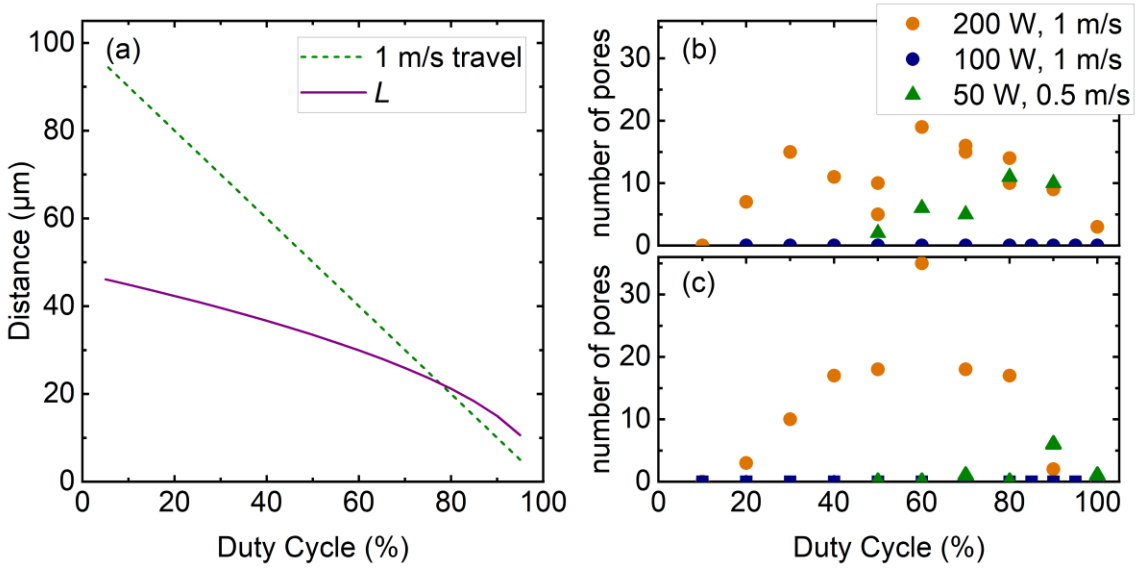

Figure 2. Porosity and thermal effects in modulated melting. a) Comparison of distance travelled when the laser is off at 1 m/s and thermal diffusion length *L*. Pores observed in single track melting *in situ* X-ray imaging experiments at (b) 10 kHz modulation frequency with 9 modulation cycles and (c) 20 kHz modulation frequency with 18 modulation cycles. These experiments used Ti-64 substrates and no powder. Reported laser power values indicate peak commanded laser power.

Figure 2b and 2c illustrate number of pores observed over the central 1 mm of a 3 mm long single laser scan in Ti-64 for a variety of peak power values at 10 kHz and 20 kHz modulation frequencies as a function of duty cycle. In both cases, the 100 W, 1 m/s scan produces no pores because that power and speed combination does not produce the deep, unstable keyhole conditions required to trap pores. For 200 W peak power, the situation is different. Under continuous wave (CW) conditions (100% duty cycle), few pores are formed. Immediately upon the introduction of power modulation, pores begin to form. The amount of pores remains small at high duty cycle, in particular at 20 kHz where the laser off time remains low. The number of pores steadily increases until it reaches a relative plateau at intermediate duty cycle. This plateau occurs because pore formation is primarily caused by the collapse of the vapor cavity when the laser turns off at the end of each modulation cycle. Therefore, the number of modulation cycles has a stronger influence on the number of pores than the duty cycle during that plateau. As duty cycle further decreases, the amount of porosity begins to steadily decrease until no more pores are formed at the lowest duty cycles. Each of these regimes are described in more detail below.

B. Regime 1: Vapor depression at high duty cycle

Even at the highest duty cycles investigated, the behavior of the melt pool is drastically different during processing with microsecond pulsing when compared to CW laser melting. Unlike CW laser melting, melt pool behavior is transient due to the modulation of the laser heat source and the melt pool never reaches a steady state. The vapor depression is extremely sensitive to changes to the laser heat source on microsecond timescales. Figure 3a illustrates changes in the vapor depression depth as a function

of time for CW laser melting and 90% duty cycle with a peak laser power of 100 W at 10 kHz modulation frequency. The vapor depression depth in the CW case is relatively constant, with an average depth of ~87 μm. In the 90% duty cycle case, the vapor depression fluctuates between ~20 μm to ~96 μm deep, depending on the point in the pulse cycle. The laser turns on when the depression is at ~20 μm, and the depression grows deeper for the duration of the 90 μs on time. asymptotically approaching the deepest point. The vapor depression reaches the deepest point at the end of the laser pulse, 96 μm on average. After the laser turns off, the vapor depression immediately collapses to ~20 μm deep, and the cycle repeats. A continuous melt pool is maintained, and no substantial melt ejections are observed when the laser turns on for each pulse. This rapid vapor depression collapse does not generate any additional pores in the high duty cycle regime. In cases where pores do form, such as at 200 W and 1 m/s in Ti-64, the pore formation mechanisms are due to stochastic instabilities in the vapor depression similar to how pores are formed in keyhole mode processing for CW laser melting.

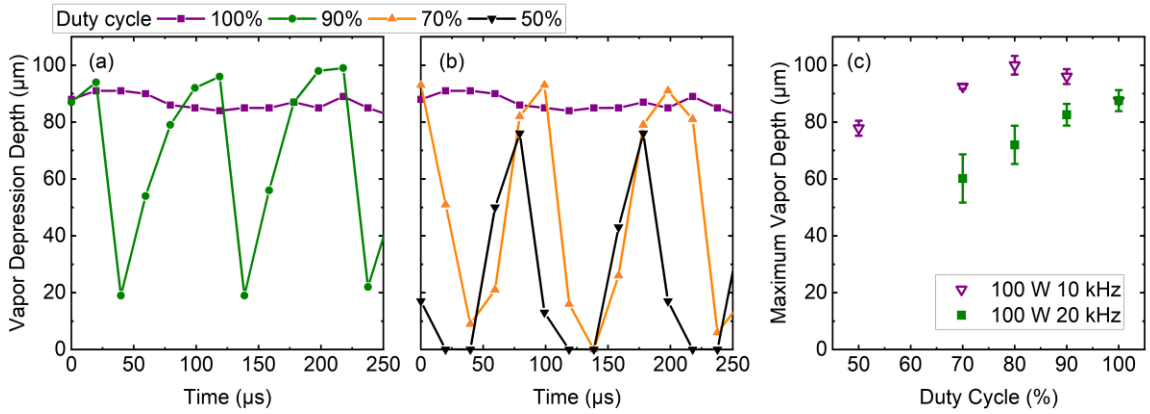

Figure 3. Vapor depression depths as a function of time in Ti-64 with a peak laser power of 100 W at a scan speed of 1 m/s. (a) Comparison of vapor depression depth for steady state CW laser melting (100% duty cycle) and 90% duty cycle. (b) Comparison of vapor depression depth for 70% and 50% duty cycle melting. The steady state CW data (100% duty cycle) is the same as that shown in panel (a). (c) Maximum vapor depression depth as a function of duty cycle. Each data point is the average of the deepest observed point for each pulse cycle, and error bars indicate standard deviation of ~6 cycles for 10 kHz data and ~12 cycles for 20 kHz.

Interestingly, the maximum vapor depression depth at 10 kHz for high duty cycles exceeds the vapor depression depth in CW melting (Figure 3c) despite the lower average power. This is not true for 20 kHz pulse formats. This difference between modulation frequency is due to the difference in overall pulse length, as the shorter pulses in the 20 kHz case do not allow sufficient time for the vapor depression to reach the maximum depth observed in longer pulses. Notably, this behavior is also not observed at the start of laser strikes in CW laser scanning.[57] Assuncao and Williams also observed deeper penetration in microsecond/millisecond pulsed welding than in CW welding.[29] They claimed that melt pool flow counteracts the recoil pressure and reduces the vapor depression depth in the CW case, where the laser interacts with the liquid melt. They claim that the melt pool solidified between pulses such that the laser interacted with a stationary solid rather than a pre-existing melt pool, leading

to increased depth because of a lack of fluid flow to counteract recoil pressure. This mechanism does not apply in the case reported here, where the melt pool does not fully solidify between pulses at the high duty cycle where we observe increased penetration.

C. Regime 2: intermediate duty cycle

Flow behavior changes significantly at intermediate duty cycle, when pores and other defects begin to form due to the laser modulation. These defects include subsurface porosity, surface divots, and large spatter events (not shown) arising from each laser pulse that could lead to lack of fusion defects elsewhere in a full part build.[58] The relative magnitude of these defects depends on laser power, scan speed, and duty cycle. For example, porosity is not observed under the regime of lower peak laser powers.

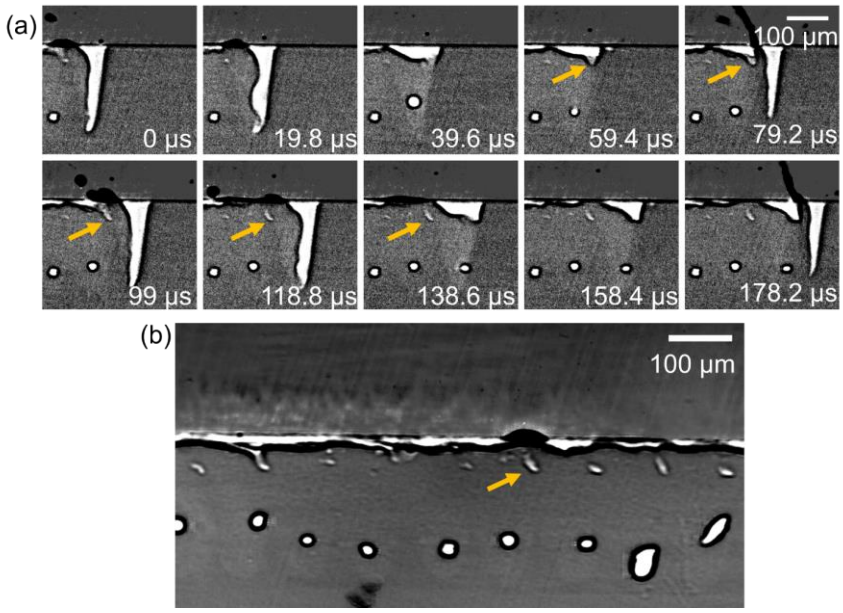

Figure 4 Pore formation in Ti-64 at intermediate duty cycle. (a) Time series of X-ray difference images during laser melting illustrating pore formation events at a laser peak power of 200 W, scan speed of 1 m/s, and laser modulation at 10 kHz with a 70% duty cycle. (b) Difference image from the same laser scan shown in (a) after laser melting. The yellow arrow points to the same pore location in all images.

As in the high duty cycle regime, the vapor depression motion and behavior depends heavily on laser power (Figure 3b). When the laser turns off, the vapor depression rapidly collapses because the recoil pressure maintaining the depression vanishes when the laser heat source is removed. In cases where the laser power is sufficiently high to generate a deep vapor depression, the base of this vapor depression collapses to form a pore, as often happens at the end of laser scan tracks in CW processing.[40] The shape of these pores depends on the frequency of the laser modulation, the material properties, and the laser power and ranges from nearly spherical (Figure 4) to more oblong (Figure 5, 6). Since these pore formation events are tied to the laser turning off rather than the length of time

the laser is on, pore count remains relatively constant across a wide range of intermediate duty cycles at a given modulation frequency. After vapor depression collapse, the laser is off for long enough for the vapor depression to vanish and for the melt pool to freeze completely. In some cases, this also corresponds to surface freezing where a depression remains present but is frozen in place by the solidifying melt pool. When the laser turns on again, the interaction with the solidified substrate generates a very large melt pool protrusion that leads to a spatter ejection directed backwards relative to the laser scan direction, similar to what occurs at the start of the track when the laser first fires in CW laser processing.[57] The newly created melt pool re-melts portions of the previously present laser track, leading to a continuous molten region at the end of the process even though the melt pool was not necessarily continuously present. For some processing conditions, this large melt protrusion is only partially ejected, and the remainder falls back to cover the frozen vapor depression and create a pore (Figure 4). In other cases, this backwards protrusion fully fills the depression left from the previous frozen vapor depression and does not create a pore. At lower duty cycles, unfilled surface divots are more common.

There are notable differences in behavior between 10 kHz and 20 kHz modulation frequencies reflected in the total number of pores formed during scanning in this regime (Figure 2b and 2c). Figures S5 and S6 in the Supplementary Information show X-ray images of the post-scan condition for each duty cycle that showed periodic pore formation with a laser power of 200 W and a scan speed of 1 m/s. In spite of the fact that the fixed field of view for our experiment leads to twice as many modulation cycles at 20 kHz than at 10 kHz, a similar number of pores are observed between the two because at 10 kHz far more small, near-surface pores are formed during vapor depression collapse. These near-surface pores are in addition to what tends to be a single larger pore near the base of the vapor depression trapped at each laser off instance. These pores are far less common at 20 kHz because for a given scan speed, the distance travelled during each modulation cycle is half that of the 10 kHz case, so the following laser pulse disrupts small near-surface pores. For example, at 1 m/s the travel distance at 20 kHz is only 50 μm, smaller than the diameter of the build laser. These surface instabilities are more stochastic than the pores generated at the base of the vapor depression, leading to a more consistent plateau in the number of pores per modulation cycle at 20 kHz than what is observed at 10 kHz. The exception to this trend in the 20 kHz case, at 60% duty cycle, corresponds to the only observed case where the balance between duty cycle and travel time lead to those near-surface pores being preserved at 20 kHz. The plateau in number of pores at 20 kHz between 80% and 40% duty cycle corresponds to depositing one subsurface pore per laser modulation cycle, suggesting that this behavior could be exploited to insert controlled porosity in LPBF parts.

D. Regime 3: low duty cycle

At low duty cycle, the process is better viewed as a series of consecutive and adjacent but independent spot welds. In these instances, the vapor depression collapse and melt freezing is too rapid to be captured by our 50.4 kfps frame rate (Figure 5). As is the case at intermediate duty cycle, each laser strike induces the ejection of a significant jet of molten metal, and a vapor depression is present. The vapor depression freezes to leave a significant surface divot and a subsurface pore in cases where the

vapor depression is sufficiently deep because of the laser power. These trapped pores are vertically elongated, occur very regularly at each laser strike point, and do not occur at lower laser powers. In some cases, these pores do not fully pinch off from the surface divot and are instead a larger, deep cavity connected to the surface divot by a thin neck rather than true fully-enclosed pores.

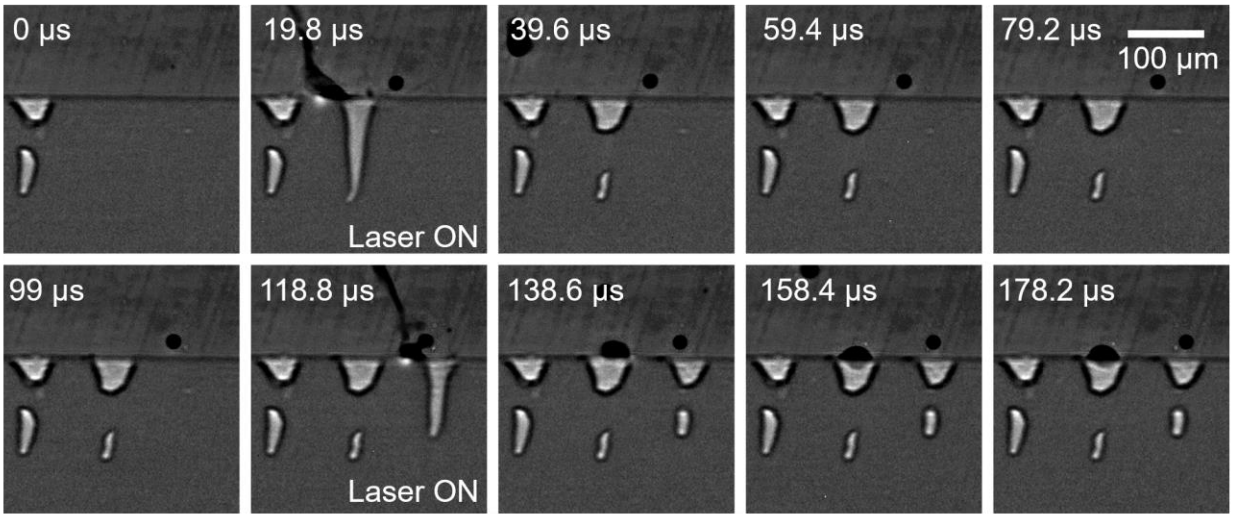

Figure 5 Pore formation in Ti-64 at low duty cycle, using a peak laser power of 200 W, scan speed of 1 m/s and modulation frequency of 10 kHz with a 20% duty cycle.

E. Material Dependence and scaling

The overall behavior observed in Ti-64 also occurs in both 316L steel and Al1100. While all three regimes are observed in each material, many of the details of materials behavior, such as defect and melt ejection morphology and laser parameters corresponding to each defect formation regime vary as a function of the specific material properties. These differences in behavior are highlighted in Figure 6, which compares pore and surface divot morphology for 316L steel, Al1100, and Ti-64 substrates produced with a peak laser power of 200 W, scan speed of 1 m/s, modulation frequency of 10 kHz, and 50% duty cycle. Pore depth correlates strongly with melt depth and therefore is governed by well-established scaling relationships for LPBF. The morphology of pores and surface divots is determined by the dynamics of fluid flow after the laser shuts off during each modulation cycle. These dynamics primarily depend on a combination of surface tension and viscosity of the liquid metal and are therefore strongly influenced by oxygen concentration as well as the major alloy constituents. Another critical parameter is the amount of time the melt pool remains liquid between when the vapor depression collapses to form a vapor bubble and when the solidification front passes through this bubble, trapping it as a pore. This is governed by the solidification front velocity as well as the temperature difference between the boiling and freezing temperature for the alloy. For the conditions studied here the solidification front velocities are approximately the same order of magnitude across the conditions we explore, and the difference between boiling and freezing temperature are also on the same order of magnitude: ~1390 K for 316L,[59] 1860K for pure Al,[60] and 1900 K for pure Ti.[61]

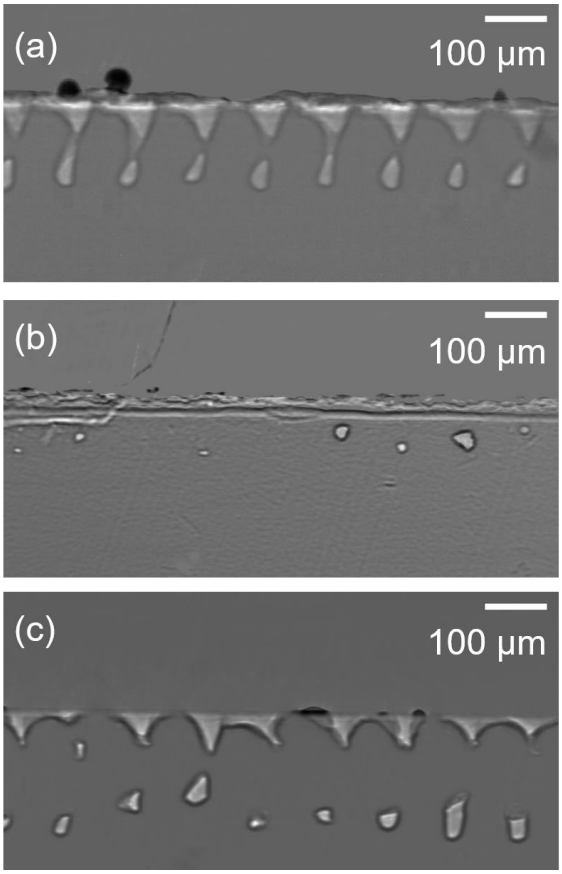

Figure 6 Material dependence of pore and surface divot morphology for a laser peak power of 200 W, scan speed of 1 m/s, and a 10 kHz modulation frequency at 50% duty cycle. (a) 316L steel. (b) Al1100. (c) Ti-64.

Changes to melt behavior as a function of material is expected, as material-dependent scaling laws for CW laser melting are well established and can accurately predict melt pool depth, the onset of keyhole-mode melting, and keyhole porosity formation.[37, 62-65] However, existing scaling laws developed for CW melting are based on assumptions of steady-state melting conditions and therefore are not necessarily directly applicable to pulsed laser melting presented here, because the melt pool never reaches a steady state condition. However, at high duty cycle the heat flux near the edges of the melt pool likely reaches a near-steady state condition, so these steady state assumptions may hold. Here we explore the limits of the normalized enthalpy relationship[63-65] to determine if this scaling approach still applies to the transient behavior present in modulated laser melting. The normalized enthalpy scaling law for steady-state melting is given Equation 3:

$$\frac{\Delta H}{h_s} = \frac{AP}{\pi \rho C T_m \sqrt{D v \sigma^3}} \quad [3]$$

Where $\frac{\Delta H}{h_s}$ is the normalized enthalpy, or the change in enthalpy ΔH divided by the enthalpy at melting h_s, A absorptivity, P is average laser power, ρ is density, C is heat capacity, T_m is melt temperature, D is thermal diffusivity, v is scan velocity, and σ is $1/e^2$ beam radius. Enthalpy at melting is equivalent to

$h_s = \rho C T_m$. Here we use the same form, but with some slight modifications to specific terms to account for changes to the process induced by modulating the laser power. Most materials properties variables are independent of the laser pulse format so ρ, C, T_m, and D remain unchanged. However, the laser absorptivity value A likely changes as a function of the pulse format and duration, making robust scaling difficult. Absorptivity values depend heavily on the geometry of the vapor depression on the surface of the melt pool,[66, 67] and are particularly sensitive to the vapor depression depth.[68, 69] The rapid changes to vapor depression geometry on short timescales discussed above suggest that the absorptivity dynamically changes during the 10-100 μs long laser pulses studied here due to multiple-reflection effects.[69] For accurate scaling, it is critical to use the correct time-averaged value for A, which will depend not only on laser power and scan speed, as shown in previous studies,[13, 64] but also on pulse duration and frequency.

A subset of samples were cross sectioned for metallography melt pool depth measurements, which are shown in Figure 7. These melt depth values were measured from cross sections of a subset of samples generated in the X-ray imaging experiment. For these calculations, absorptivity values of A = 0.56 for Ti-64 and A = 0.6 for 316L steel were used was used based on data from Ye *et al*[64] at comparable CW process parameters. The data point at 20 kHz sampling exhibits a lower melt pool depth than an equivalent duty cycle for 10 kHz cases, which is likely due to a reduced average absorptivity caused by lower vapor depression depths at higher modulation frequency (see Figure 3c). This discrepancy suggests that differences in dynamic vapor depression geometry at different duty cycles strongly influence time-averaged absorptivity value and limits the accuracy of this scaling calculation.

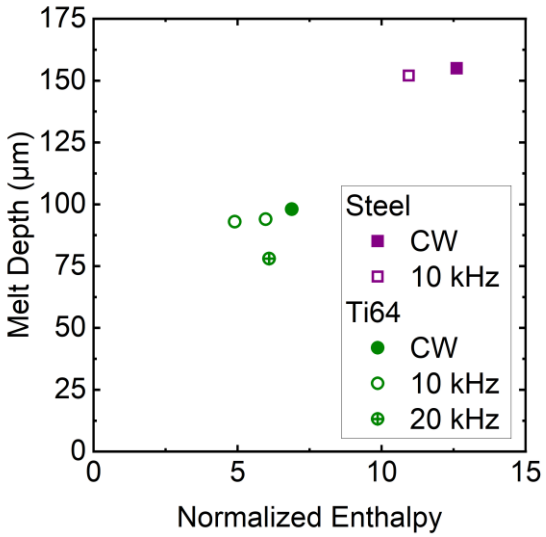

Figure 7 Melt pool depth as a function of normalized enthalpy for experiments using 1 m/s scan speed at 80% and 90% duty cycle. The Ti-64 samples used 100 W and 316L 200 W.

F. Influence of powder

The previous discussion focuses on bare plate experiments, which are valuable for understanding the laser-material interaction but cannot quantify the influence of powder on melt dynamics. Therefore, we performed complimentary experiments with powder to confirm that the behavior observed in the bare plate cases translates to LPBF build conditions that include a powder layer. Figure 8 compares pore formation in Ti-64 with and without powder at 1 m/s scan speed. The introduction of powder does not significantly influence the duty cycle dependence of pore formation. While pore formation begins at slightly higher duty cycle in the bare plate case, the overall behavior remains qualitatively similar. Detailed surface wave behavior and start of track melt ejection in the powder case is obscured by the powder layer, but vapor depression behavior is quite similar to the bare plate case so it is likely that the melt pool surface flow behaviors are similar as well.

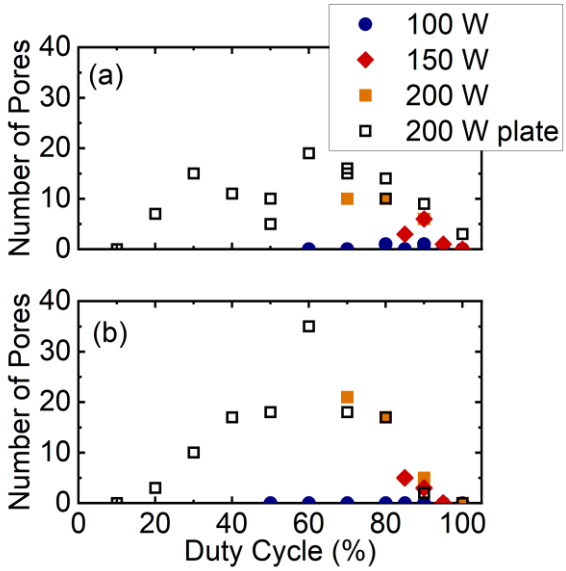

Figure 8 Influence of powder on pore formation in Ti-64 at a scan speed of 1 m/s. (a) Porosity as a function of duty cycle at 10 kHz with powder, with a 200 W plate case as a comparison. (b) Porosity as a function of duty cycle at 20 kHz.

In addition to analyzing the influence of powder on melt pool and fluid flow behavior, the behavior of the powder itself is important to understanding contrasts between CW and pulsed melting. The dependence between powder denudation has been well established as a function of ambient pressure,[6, 70] but powder motion and denudation behavior under pulsed laser melting conditions is less well investigated. X-ray imaging data permit the observation of a 2-dimensional projection of powder and spatter motion. This provides valuable insight into how ejections relate to subsurface melt behavior but limits the conclusions that can be drawn when evaluating powder motion alone, as motion parallel to the X-ray beam cannot be distinguished. Control experiments with 100 W, CW melting in Ti-64 at 1 m/s (100% duty cycle) exhibit behavior broadly similar to previous reports.[7, 46] Powder is pushed forward in front of the laser beam and large spatter particles are ejected in various directions near the vapor depression. Powder moves upward slightly behind the vapor depression and there is additional motion in the powder layer itself, likely related to the denudation effect,[6] but since denudation motion

is largely perpendicular to the laser scan direction and parallel to the X-ray beam, this motion cannot be analyzed in detail from X-ray images alone. At high duty cycle (80-90% duty cycle for both 10 kHz and 20 kHz pulse frequencies), powder motion during pulsed melting does not exhibit significant differences when compared to CW melting. At lower duty cycle (60-70% for 20 kHz, 70% for 10 kHz), more large spatter ejection events are evident than is the case in CW melting, but these arise from the start of track ejections observed in the bare plate case and are unrelated to the presence of powder. Powder motion other than these melt ejections remains broadly similar to the CW and higher duty cycle cases. At lower duty cycles, regimes that are unattractive for full scale printing due to melt pool behavior and pore formation, the powder motion visible in the X-ray imaging begins to exhibit substantial differences from CW melting. At 50% duty cycle and 20 kHz, more powder is ejected vertically from the substrate surface. At 60% duty cycle and 10 kHz, in contrast, substantially less powder is ejected, and the powder ejection events correspond to specific laser pulses. When the laser fires, powder is ejected near the location of the laser strike, but powder outside 100 – 150 μm is not displaced.

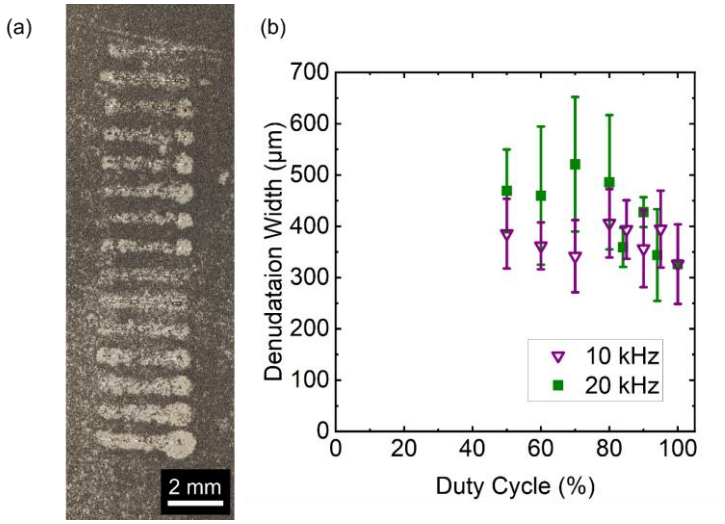

Figure 9. Width of the denudation zone. (a) microscope image after laser melting illustrating differences in denudation zones as a function of pulse parameters. (b) Denudation zone width measurements as a function of duty cycle for 10 and 20 kHz modulation frequencies.

To evaluate powder motion in the plane of the powder bed, we performed high speed optical imaging experiments at a scan speed of 1 m/s and a peak laser power of 100 W with the same pulse formats that were used for the X-ray imaging. The results are broadly consistent with what is observed in the X-ray imaging data. In CW melting, denudation behavior is consistent with previous reports. Powder is drawn towards the single track behind the melt pool due to gas entrainment. For pulsed melting, the in-plane powder motion and resulting denudation depends substantially on the frequency of the pulsing. At 10 kHz modulation frequency, powder motion appears broadly similar to the CW case with powder swept towards the laser scan line behind the melt pool due to vapor entrainment. The width of the denudation zone, measured via *ex situ* microscopy, remains relatively constant down to 50% duty cycle (Figure 9). At 20 kHz modulation frequency, however, powder motion is substantially

different. At duty cycles above 80%, denudation behavior does not substantially differ from CW. At lower duty cycles, however, powder motion exhibits less and less entrainment behavior and begins to be dominated by powder expulsion at the start of the pulse. This also leads to larger denudation zones, because the initial laser strike causes a vapor jet that expels powder, but then before that vapor jet can cause substantial entrainment the laser pulse stops and the vapor jet decays. This effect is more prevalent at 20 kHz than at 10 kHz because the laser pulse durations are half as long for a given duty cycle, so the dynamics during the initial laser strike dominate overall behavior.

IV. Conclusions

This article reports *in situ* X-ray experiments that probe melt pool fluid flow and defect formation behavior unique to modulated laser melting during LPBF. While pulsing adds duty cycle as an additional dimension to the process window for producing fully dense parts, reducing duty cycle too far results in unique pore formation mechanisms that prevent high quality part production. Our experiments show that the time between laser pulses has the most significant influence on pore formation, and longer laser off times correlate with a greater likelihood of defect formation. This is because with long laser off times, the laser pulse strikes a solidified substrate, which causes a start of track type ejection and traps pores. Such large ejection events do not occur when the laser strikes a pre-existing melt pool. We also apply the commonly used normalized enthalpy scaling approach to understand variation between different materials and show that modifications to accommodate modulation frequency must also account for changes to absorptivity caused by changes to vapor depression shape as a function of modulation. Finally, we observe that for specific laser pulse conditions it is possible to deterministically create one subsurface pore per laser pulse, which provides a powerful approach to control porosity and intentionally build in failure points at specific locations during a build.

Supplementary Material

The supplementary material includes details of the actual laser output compared to the commanded behavior. It also contains additional X-ray image data.

Acknowledgements

This work was performed under the auspices of the U.S. Department of Energy (DOE) by Lawrence Livermore National Laboratory (LLNL) under Contract No. DE-AC52–07NA27344. It was supported by the LLNL LDRD program (project 17-ERD-042). This research used resources of the Advanced Photon Source, a DOE Office of Science User Facility operated for the DOE Office of Science by Argonne National Laboratory under contract no. DE-AC02-06CH11357. We acknowledge experimental assistance at APS sector 32 from Alex Deriy and Kamel Fezzaa, and fabrication assistance form the LLNL precision machine shop. We also acknowledge helpful discussions with Ben Brown.

References

1. W. J. Keller, N. Shen, A. M. Rubenchik, S. Ly, R. Negres, R. N. Raman, J.-H. Yoo, G. Guss, J. S. Stolken, M. J. Matthews and J. D. Bude, Journal of Applied Physics **125** (8) (2019).
2. X. He, J. W. Elmer and T. DebRoy, Journal of Applied Physics **97** (8) (2005).
3. Y. Kawahito, M. Kito and S. Katayama, Journal of Physics D: Applied Physics **40** (9), 2972 (2007).
4. K. A. Mumtaz and N. Hopkinson, Journal of Materials Processing Technology **210** (2), 279-287 (2010).
5. A. R. Nassar and E. W. Reutzel, Metallurgical and Materials Transactions A **46** (6), 2781-2789 (2015).
6. M. J. Matthews, G. Guss, S. A. Khairallah, A. M. Rubenchik, P. J. Depond and W. E. King, Acta Materialia **114**, 33-42 (2016).
7. S. Ly, A. M. Rubenchik, S. A. Khairallah, G. Guss and M. J. Matthews, Scientific Reports **7** (1), 4085 (2017).
8. P. Bidare, I. Bitharas, R. M. Ward, M. M. Attallah and A. J. Moore, Acta Materialia **142**, 107-120 (2018).
9. I. Bitharas, A. Burton, A. J. Ross and A. J. Moore, Additive Manufacturing **37**, 101690 (2021).
10. A. R. Nassar, M. A. Gundermann, E. W. Reutzel, P. Guerrier, M. H. Krane and M. J. Weldon, Scientific Reports **9** (1), 5038 (2019).
11. P. A. Hooper, Additive Manufacturing **22**, 548-559 (2018).
12. B. Lane, I. Zhirnov, S. Mekhontsev, S. Grantham, R. Ricker, S. Rauniyar and K. Chou, Additive Manufacturing **36**, 101504 (2020).
13. J. Trapp, A. M. Rubenchik, G. Guss and M. J. Matthews, Applied Materials Today **9**, 341-349 (2017).
14. S. N. Luo, S. D. C., T. I. V. T. E., P. D. L., K. G. A., J. R. P., H. A. A., T. O. and P. D. and Asimow, High Pressure Research **24** (4), 409-422 (2004).
15. M. P. Olbinado, V. Cantelli, O. Mathon, S. Pascarelli, J. Grenzer, A. Pelka, M. Roedel, I. Prencipe, A. L. Garcia, U. Helbig, D. Kraus, U. Schramm, T. Cowan, M. Scheel, P. Pradel, T. De Resseguier and A. Rack, Journal of Physics D: Applied Physics **51** (5), 055601 (2018).
16. M. G. Gorman, R. Briggs, E. E. McBride, A. Higginbotham, B. Arnold, J. H. Eggert, D. E. Fratanduono, E. Galtier, A. E. Lazicki, H. J. Lee, H. P. Liermann, B. Nagler, A. Rothkirch, R. F. Smith, D. C. Swift, G. W. Collins, J. S. Wark and M. I. McMahon, Physical Review Letters **115** (9), 095701 (2015).
17. D. Devaux, R. Fabbro, L. Tollier and E. Bartnicki, Journal of Applied Physics **74** (4), 2268-2273 (1993).
18. P. Peyre and R. Fabbro, Optical and Quantum Electronics **27** (12), 1213-1229 (1995).
19. S. Ly, G. Guss, A. M. Rubenchik, W. J. Keller, N. Shen, R. A. Negres and J. Bude, Scientific Reports **9** (1), 8152 (2019).
20. L. Caprio, A. G. Demir and B. Previtali, Journal of Materials Processing Technology **266**, 429-441 (2019).
21. S. Ghouse, S. Babu, R. J. Van Arkel, K. Nai, P. A. Hooper and J. R. T. Jeffers, Materials & Design **131**, 498-508 (2017).
22. S. Ghouse, S. Babu, K. Nai, P. A. Hooper and J. R. T. Jeffers, Additive Manufacturing **22**, 290-301 (2018).
23. A. G. Demir and B. Previtali, Materials & Design **119**, 338-350 (2017).
24. L. Caprio, A. G. Demir and B. Previtali, Journal of Laser Applications **30** (3) (2018).

25. B. Brown, J. Newkirk and F. Liou, Materials **14** (3), 560 (2021).
26. F. L. Vecchiato, H. de Winton, P. A. Hooper and M. R. Wenman, Additive Manufacturing **36**, 101401 (2020).
27. S. Li, H. Xiao, K. Liu, W. Xiao, Y. Li, X. Han, J. Mazumder and L. Song, Materials & Design **119**, 351-360 (2017).
28. C. A. Biffi, J. Fiocchi, P. Bassani and A. Tuissi, Additive Manufacturing **24**, 639-646 (2018).
29. E. Assuncao and S. Williams, Optics and Lasers in Engineering **51** (6), 674-680 (2013).
30. A. Y. Alfaify, J. Hughes and K. Ridgway, Additive Manufacturing **19**, 197-204 (2018).
31. A. G. Demir, P. Colombo and B. Previtali, The International Journal of Advanced Manufacturing Technology **91** (5), 2701-2714 (2017).
32. M. Zheng, L. Wei, J. Chen, Q. Zhang, J. Li, S. Sui, G. Wang and W. Huang, Applied Surface Science **496**, 143649 (2019).
33. C. Zhao, K. Fezzaa, R. W. Cunningham, H. Wen, F. De Carlo, L. Chen, A. D. Rollett and T. Sun, Scientific Reports **7** (1), 3602 (2017).
34. N. P. Calta, J. Wang, A. M. Kiss, A. A. Martin, P. J. Depond, G. M. Guss, V. Thampy, A. Y. Fong, J. N. Weker, K. H. Stone, C. J. Tassone, M. J. Kramer, M. F. Toney, A. Van Buuren and M. J. Matthews, Review of Scientific Instruments **89** (5) (2018).
35. C. L. A. Leung, S. Marussi, R. C. Atwood, M. Towrie, P. J. Withers and P. D. Lee, Nature Communications **9** (1), 1355 (2018).
36. T. Sun, W. Tan, L. Chen and A. Rollett, MRS Bulletin **45** (11), 927-933 (2020).
37. A. A. Martin, N. P. Calta, S. A. Khairallah, J. Wang, P. J. Depond, A. Y. Fong, V. Thampy, G. M. Guss, A. M. Kiss, K. H. Stone, C. J. Tassone, J. Nelson Weker, M. F. Toney, T. van Buuren and M. J. Matthews, Nature Communications **10** (1), 1987 (2019).
38. C. Zhao, Q. Guo, X. Li, N. Parab, K. Fezzaa, W. Tan, L. Chen and T. Sun, Physical Review X **9** (2), 021052 (2019).
39. L. Sinclair, C. L. A. Leung, S. Marussi, S. J. Clark, Y. Chen, M. P. Olbinado, A. Rack, J. Gardy, G. J. Baxter and P. D. Lee, Additive Manufacturing **36**, 101512 (2020).
40. A. A. Martin, N. P. Calta, J. A. Hammons, S. A. Khairallah, M. H. Nielsen, R. M. Shuttlesworth, N. Sinclair, M. J. Matthews, J. R. Jeffries, T. M. Willey and J. R. I. Lee, Materials Today Advances **1**, 100002 (2019).
41. C. Zhao, N. D. Parab, X. Li, K. Fezzaa, W. Tan, A. D. Rollett and T. Sun, Science **370** (6520), 1080-1086 (2020).
42. R. Cunningham, C. Zhao, N. Parab, C. Kantzos, J. Pauza, K. Fezzaa, T. Sun and A. D. Rollett, Science **363** (6429), 849-852 (2019).
43. A. M. Kiss, A. Y. Fong, N. P. Calta, V. Thampy, A. A. Martin, P. J. Depond, J. Wang, M. J. Matthews, R. T. Ott, C. J. Tassone, K. H. Stone, M. J. Kramer, A. van Buuren, M. F. Toney and J. Nelson Weker, Advanced Engineering Materials **21** (10), 1900455 (2019).
44. N. P. Calta, A. A. Martin, J. A. Hammons, M. H. Nielsen, T. T. Roehling, K. Fezzaa, M. J. Matthews, J. R. Jeffries, T. M. Willey and J. R. I. Lee, Additive Manufacturing **32**, 101084 (2020).
45. N. Kouraytem, X. Li, R. Cunningham, C. Zhao, N. Parab, T. Sun, A. D. Rollett, A. D. Spear and W. Tan, Physical Review Applied **11** (6), 064054 (2019).
46. Q. Guo, C. Zhao, L. I. Escano, Z. Young, L. Xiong, K. Fezzaa, W. Everhart, B. Brown, T. Sun and L. Chen, Acta Materialia **151**, 169-180 (2018).
47. Q. Guo, C. Zhao, M. Qu, L. Xiong, S. M. H. Hojjatzadeh, L. I. Escano, N. D. Parab, K. Fezzaa, T. Sun and L. Chen, Additive Manufacturing **31**, 100939 (2020).
48. A. Matsunawa, N. Seto, M. Mizutani and S. Katayama, presented at the ICALEO '98: Proceedings of the Laser Materials Processing Conference, 1998 (unpublished).

49. S. Shevchik, T. Le-Quang, B. Meylan, F. V. Farahani, M. P. Olbinado, A. Rack, G. Masinelli, C. Leinenbach and K. Wasmer, Scientific Reports **10** (1), 3389 (2020).
50. K. Wasmer, T. Le-Quang, B. Meylan, F. Vakili-Farahani, M. P. Olbinado, A. Rack and S. A. Shevchik, Procedia CIRP **74**, 654-658 (2018).
51. N. H. Paulson, B. Gould, S. J. Wolff, M. Stan and A. C. Greco, Additive Manufacturing **34**, 101213 (2020).
52. S. Gorgannejad, A. A. Martin, J. W. Nicolino, M. Strantza, G. M. Guss, S. Khairallah, J.-B. Forien, V. Thampy, S. Liu, P. Quan, C. J. Tassone and N. P. Calta, Additive Manufacturing **78**, 103810 (2023).
53. S. M. H. Hojjatzadeh, Q. Guo, N. D. Parab, M. Qu, L. I. Escano, K. Fezzaa, W. Everhart, T. Sun and L. Chen, Materials **14** (11), 2936 (2021).
54. S. Tsukamoto, I. Kawaguchi, G. Arakane and H. Honda, presented at the ICALEO 2001: Proceedings of the Laser Materials Processing Conference and Laser Microfabrication Conference, 2001 (unpublished).
55. M. B. von Allmen, *Laser-beam Interactions with Materials*. (SPringer-Verlang, New York, 1995).
56. M. Boivineau, C. Cagran, D. Doytier, V. Eyraud, M. H. Nadal, B. Wilthan and G. Pottlacher, International Journal of Thermophysics **27** (2), 507-529 (2006).
57. S. A. Khairallah, A. A. Martin, J. R. I. Lee, G. Guss, N. P. Calta, J. A. Hammons, M. H. Nielsen, K. Chaput, E. Schwalbach, M. N. Shah, M. G. Chapman, T. M. Willey, A. M. Rubenchik, A. T. Anderson, Y. M. Wang, M. J. Matthews and W. E. King, Science **368** (6491), 660-665 (2020).
58. Z. Snow, L. Scime, A. Ziabari, B. Fisher and V. Paquit, Additive Manufacturing **61**, 103298 (2023).
59. C. S. Kim, 1975.
60. P. D. Desai, International Journal of Thermophysics **8** (5), 621-638 (1987).
61. J. Black and G. Hastings, in *Handbook of Biomaterial Properties*, edited by J. Black and G. Hastings (Springer US, Boston, MA, 1998), pp. 179-200.
62. D. B. Hann, J. Iammi and J. Folkes, Journal of Physics D: Applied Physics **44** (44), 445401 (2011).
63. A. M. Rubenchik, W. E. King and S. S. Wu, Journal of Materials Processing Technology **257**, 234-243 (2018).
64. J. Ye, S. A. Khairallah, A. M. Rubenchik, M. F. Crumb, G. Guss, J. Belak and M. J. Matthews, Advanced Engineering Materials **21** (7), 1900185 (2019).
65. W. E. King, H. D. Barth, V. M. Castillo, G. F. Gallegos, J. W. Gibbs, D. E. Hahn, C. Kamath and A. M. Rubenchik, Journal of Materials Processing Technology **214** (12), 2915-2925 (2014).
66. B. J. Simonds, J. Tanner, A. Artusio-Glimpse, P. A. Williams, N. Parab, C. Zhao and T. Sun, Procedia CIRP **94**, 775-779 (2020).
67. S. A. Khairallah, T. Sun and B. J. Simonds, Additive Manufacturing Letters **1**, 100002 (2021).
68. T. R. Allen, W. Huang, J. R. Tanner, W. Tan, J. M. Fraser and B. J. Simonds, Physical Review Applied **13** (6), 064070 (2020).
69. B. J. Simonds, J. Sowards, J. Hadler, E. Pfeif, B. Wilthan, J. Tanner, C. Harris, P. Williams and J. Lehman, Physical Review Applied **10** (4), 044061 (2018).
70. P. Bidare, I. Bitharas, R. M. Ward, M. M. Attallah and A. J. Moore, International Journal of Machine Tools and Manufacture **130-131**, 65-72 (2018).